Coupled Systems Mechanics, *Vol. 14, No. 3 (2025) 269-288*
https://doi.org/10.12989/csm.2025.14.3.269

Parametric dynamic instability of a suspension bridge deck under dynamic loading along two of its opposite edges

Hafid Mataich*

Laboratory of Informatics and Interdisciplinary Physics (LIPI), High Normal School, Sidi Mohamed Ben Abdellah University, 30040 Fez, Morocco

(Received March 6, 2025, Revised June 20, 2025, Accepted July 9, 2025)

Abstract. This paper examines the dynamic instability of a suspension bridge deck, modeling it as a symmetrically laminated rectangular plate made of composite material, featuring an angular fold and subject to various boundary conditions. To simplify the analysis, the instability of this structure is studied under the effect of a dynamic, non-uniform and periodic uni-axial loading applied along its edges. The equations of motion are formulated using Reissner-Mindlin's first-order shear deformation theory (FSDT) and Hamilton's principle. FSDT is based on five degrees of freedom (DOF) modeling per node within a finite element approach. Structural damping, modeled using the Rayleigh method, is incorporated into the system of equations to assess its influence on instability characteristics. A modal analysis is then performed to decouple the partial differential equations (PDEs) into a Mathieu-Hill system of ordinary differential equations (ODEs), thus reducing the problem size. The dynamic instability zones (DIR) of the plate are identified by applying the Bolotin approach, while the dynamic excitation frequencies are determined by solving an eigenvalue problem. Finally, a parametric analysis is carried out to examine the influence of the various parameters on the lower and upper bounds of the instability zones, as well as on the simple parametric resonance phenomenon of the structure representing the deck.

Keywords: Bolotin approach; dynamic instability; dynamic load; Mathieu-Hill equations; Runge Kutta algorithm; suspension bridge deck

1. Introduction

This study models the bridge deck as a symmetrically laminated rectangular plate with an angular fold, taking into account various boundary conditions to simulate dynamic loading induced by seismic forces. The analysis examines the effect of elastic material properties, plate geometry and the nature of dynamic loads on the dynamic instability of the structure. These results are aimed at optimizing bridge design in a cost-effective way. The instability of laminated plates has been extensively studied in the literature. Using first-order shear deformation theory (FSDT), Cong *et al.* (2021) explored the static instability of functionally graded plates, while Civalek *et al.* (2020) studied the static stability and free vibrations of composite laminated plates. The dynamic instability of laminated plates under dynamic loads applied to the edges was analyzed by Mataich

*Corresponding author, Ph.D., E-mail: Mailhafid.mataich@usmba.ac.ma

http://www.techno-press.org/?journal=csm&subpage=8 ISSN: 2234-2184 (Print), 2234-2192 (Online)

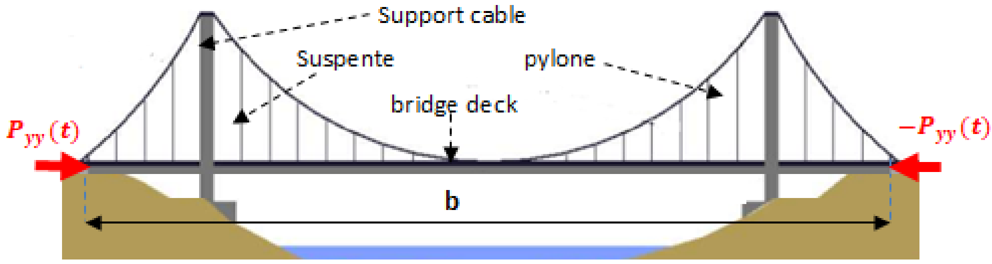

Fig. 1 Diagram of a suspension bridge showing dynamic effects in the deck plane $P_{yy}(t)$

and El Amrani (2023), Partha and Singha (2006), Zarina *et al.* (2020), Jinhua *et al.* (2019), Dadakhan *et al.* (2020). The effect of non-uniform loads applied at the edges on the dynamic behavior of laminated composite plates has been studied by Balakrishna and Singh (2020), El Amrani *et al.* (2023), Kim and Kim (2000), Rajanna *et al.* (2017). The influence of damping on the dynamic instability of plane-loaded plates has been explored by Kumar *et al.* (2013), Hoseinzadeh and Rezaeepazhand (2016). Syntheses of methods for analyzing dynamic plate instability as well as potential bifurcation modes are proposed by Ida Mascolo (2019), Leslie and Richard (2002), Ziener (2012). Al-Mahdi (2020), Ilyasov (2007) examined the dynamic instability of viscoelastic plates, while Sahu and Datta (2007) studied plates and shells in conservative systems. The nonlinearities and stochastic behavior of dynamic instability have been addressed by Singha and Daripa (2009), Mataich *et al.* (2024). The effects of cutouts in plates were studied by Lee (2010), while Le Wang *et al.* (2021) explored the dynamic instability of rectangular plates moving axially in a fluid.

Whatever the material used for the bridge deck, whether reinforced concrete slabs, steel plates or other structural solutions, these elements are becoming increasingly finer. Consequently, analysis of dynamic vibrations induced by phenomena such as wind, seismic movements of the ground and/or road traffic is essential. Earthquakes, in particular, exert a significant dynamic excitation on the bridge deck and must be taken into account when designing long-span suspension bridges.

In many cases, for example when ground movement affects the two opposite ends of the deck during seismic events, a dynamic load $P_{yy}(t)$ can act on the structure. As illustrated in Fig. 1, this dynamic load, applied to both sides of the deck, can lead to dynamic buckling or parametric instability, potentially resulting in significant structural damage, or even total collapse of the structure. It is therefore crucial to carry out a stability analysis of the structure under parametric loads in order to prevent such risks. However, this complex problem seems to be insufficiently addressed in current literature.

2. Mathematical formulation of the instability problem

2.1 Formulation theory

2.1.1 Displacement field, strain and stress

This is a moderately thick plate, laminated symmetrically with respect to its neutral plane, as shown in Fig. 2. The structure is subjected to dynamic seismic loads applied in its plane on two

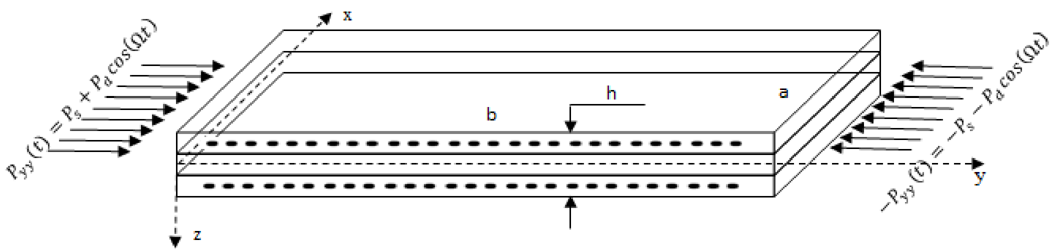

Fig. 2 Layered diagram of the bridge deck and dynamic loading in the deck plane

opposite edges. Further details are provided in Fig. 2.

According to the five-variable Reissner-Mindlin first-order shear deformation theory $u, v, w, \theta_x, \theta_y$, the displacement field of a point $M(x, y, 0, t)$ of the neutral plane is as follows as shown by Reddy (2007)

$$\begin{aligned} u_1(x,y,z,t) &= u(x,y,t) + z\theta_x(x,y,t) \\ u_2(x,y,z,t) &= v(x,y,t) + z\theta_y(x,y,t) \\ u_3(x,y,z,t) &= w(x,y,t) \end{aligned} \tag{1}$$

The displacement vector $\{d\} = \{u, v, w, \theta_x, \theta_y\}^T$ comprises displacements (u, v, w) of a point $M(x, y, 0, t)$ of the mid-plane along the axes x, y, z , respectively, as well as rotations of a normal section (θ_x, θ_y) about the *x* and *y* axes, respectively.

The membrane, bending $\varepsilon = \varepsilon^{(0)} + z\varepsilon^{(1)}$ and shear $\gamma = \gamma^{(0)}$ deformation fields are as follows

$$\varepsilon^{(0)} = [D_m]\{d\},\ \varepsilon^{(1)} = [D_b]\{d\}\ \ and\ \ \gamma^{(0)} = [D_s]\{d\} \tag{2}$$

Details of the $[D_m]$, $[D_b]$ and $[D_s]$ matrices are listed in Appendix A.

Neglecting the normal stress σ_z and using reduced elastic constants, the stress-strain relationships in the laminate frame of reference for layer number (k) are written as follows

$$\begin{Bmatrix} \sigma_m \\ \tau \end{Bmatrix}^{(k)} = \begin{bmatrix} [\bar{Q}_m] & 0 \\ 0 & [\bar{Q}_s] \end{bmatrix}^{(k)} \begin{Bmatrix} \varepsilon \\ \gamma \end{Bmatrix} \tag{3}$$

The elastic constant matrices transformed $[\bar{Q}_m]$ and $[\bar{Q}_s]$ into the laminate reference frame are detailed in Appendix A.

2.2 Guiding equation of motion

To take into account the work of non-conservative forces, the extended Hamilton principle is used, as presented by Mataich *et al.* (2024), Wang *et al.* (2021)

$$\delta \int (T - U)dt + \int \delta W_{NL}\, dt = 0 \tag{4}$$

The expression for kinetic energy is as follows

$$T = \frac{1}{2}\int_V \rho \left\{ \left(\dot{u} + z\dot{\theta}_x\right)^2 + \left(\dot{v} + z\dot{\theta}_y\right)^2 + \dot{w}^2 \right\} dV$$

$$T = \frac{1}{2}\int_{\Omega}^{\cdot}\{I_0(\dot{u}^2 + \dot{v}^2 + \dot{w}^2) + 2I_1(\dot{u}\dot{\theta}_x + \dot{v}\dot{\theta}_y) + I_2(\dot{\theta}_x^2 + \dot{\theta}_y^2)\}d\Omega$$

$$T = \frac{1}{2}\int_{\Omega}^{\cdot}\dot{d}^T[M_I]\dot{d}\, d\Omega \tag{5}$$

Where, the matrix $[M_I]$ of moments of inertia I_i is developed in appendix A, with

$$I_i = \sum_{k=1}^{NC}\int_{z_k}^{z_{k+1}}\rho z^i dz \quad for \;\; i = 1,2,3 \tag{6}$$

Strain energy due to membrane deformation, membrane-bending coupling and shear strain energy are combined in the following expression

$$U = \frac{1}{2}\int_{V}^{\cdot}\sigma^T\varepsilon dV = \frac{1}{2}\int_{V}^{\cdot}\left(\sigma_m^T\varepsilon^{(0)} + z\sigma_m^T\varepsilon^{(1)} + \tau^T\gamma^{(0)}\right)dV$$

$$U = \frac{1}{2}\int_{\Omega}^{\cdot}\{\varepsilon^{(0)T}[A]\varepsilon^{(0)} + \varepsilon^{(1)T}[B]\varepsilon^{(0)} + \varepsilon^{(0)T}[B]\varepsilon^{(1)} + \varepsilon^{(1)T}[D]\varepsilon^{(1)} + \gamma^{(0)T}[A_s]\gamma^{(0)}\}\, d\Omega \tag{7}$$

Using the material stiffness matrix expressions $[\bar{Q}_m]$ and $[\bar{Q}_s]$ provided in Appendix A, an integration through thickness is performed to obtain the plate stiffness matrix expressions.

$$A = \int_{-z/2}^{+z/2}\bar{Q}_m dz = \sum_{k=1}^{NC}\bar{Q}_m^{(k)}(z_{k+1} - z_k) \qquad B = \int_{-z/2}^{+z/2}\bar{Q}_m z dz = \sum_{k=1}^{NC}\bar{Q}_m^{(k)}\left(z_{k+1}^2 - z_k^2\right)$$

$$D = \int_{-z/2}^{+z/2}\bar{Q}_m z^2 dz = \sum_{k=1}^{NC}\bar{Q}_m^{(k)}\left(z_{k+1}^3 - z_k^3\right) \quad A_s = k\int_{-z/2}^{+z/2}\bar{Q}_s dz = k\sum_{k=1}^{NC}\bar{Q}_s^{(k)}(z_{k+1} - z_k) \tag{8}$$

The second-order potential energy, resulting from nonlinear Von Karman constraints, is determined using the displacement field of the FSDT formulation.

$$W_{NL} = \frac{1}{2}\int_{\Omega}^{\cdot}\left\{h\nabla u^T\hat{\sigma}_0\nabla u + h\nabla v^T\hat{\sigma}_0\nabla v + h\nabla w^T\hat{\sigma}_0\nabla w + \frac{h^3}{12}\nabla\theta_x^T\hat{\sigma}_0\nabla\theta_x + \frac{h^3}{12}\nabla\theta_y^T\hat{\sigma}_0\nabla\theta_y\right\}d\Omega$$

$\hat{\sigma}_0 = \begin{bmatrix}\sigma_{xx} & \sigma_{xy}\\ \sigma_{xy} & \sigma_{yy}\end{bmatrix}$ the normal and shear stresses produced by dynamic loading in the plane with $\nabla = \begin{Bmatrix}\partial_{,x}\\ \partial_{,y}\end{Bmatrix}$. In matrix form, the second-order potential energy

$$W_{NL} = \frac{1}{2}\int_{\Omega^e}^{\cdot}\{\nabla u^T\ \nabla v^T\ \nabla w^T\ \nabla\theta_x{}^T\ \nabla\theta_y{}^T\}[S_0]\begin{Bmatrix}\nabla u\\ \nabla v\\ \nabla w\\ \nabla\theta_x\\ \nabla\theta_y\end{Bmatrix}d\Omega^e \tag{9}$$

Details of the global stress matrix $[S_0]$ of dimension 10×10 are presented in Appendix A.

2.3 The boundary conditions used are as follows

In this study, we examine different types of boundary conditions in order to analyze the behavior of the plate under consideration. Two opposite edges are assumed to be free (F), while the other two opposite edges, in contact with the ground, must be subjected to rigid connections

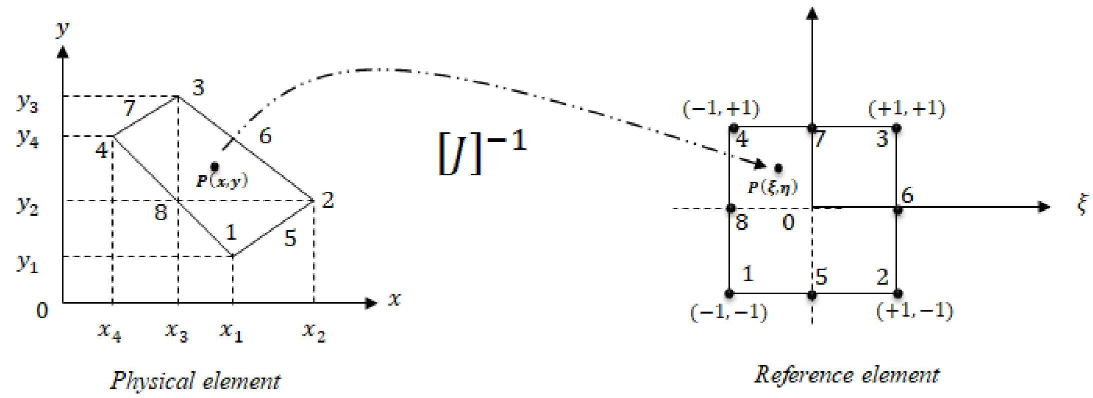

Fig. 3 Plate element representing the suspension bridge deck with 8 nodes and 5 degrees of freedom

and/or simple supports. For further details, please refer to Parveen and Harpreet (2024)

◦ (SSSS), Boundary conditions for simply supported edges,

On the $y = 0, b$ borders we have $u = w = w_{,x} = 0$

◦ (CCCC), Boundary conditions in the clamping case,

On the $y = 0, b$ borders we have $v = w = w_{,x} = w_{,y} = 0$

◦ (FFFF), Free boundary conditions :

For free boundaries (FFFF), there is no constraint for all displacements on the edges of the plate. So, on $x = 0, a$ boundaries we have. $v \neq 0$; $w \neq 0$; $w_{,x} \neq 0$; $w_{,y} \neq 0$

3. Finite element stability formulation

The plate under study will be modeled using an iso-parametric plate element with 4 or 8 nodes, as shown in Fig. 3. In line with the theory adopted previously, this element is defined by five degrees of freedom (5 DOF) per node.

Under the principle of iso-parametric elements we use interpolation functions $N_i(\eta, \xi), 1 \leq i \leq n$ to approximate both the element geometry and the five displacements, as follows

$$\begin{aligned} &x = \sum_{i=1}^{n} N_i(\eta,\xi)x_i \quad && y = \sum_{i=1}^{n} N_i(\eta,\xi)y_i \\ &u = \sum_{i=1}^{n} N_i(\eta,\xi)u_i \quad && v = \sum_{i=1}^{n} N_i(\eta,\xi)v_i \quad w = \sum_{i=1}^{n} N_i(\eta,\xi)w_i \\ &\theta_x = \sum_{i=1}^{n} N_i(\eta,\xi)\theta_{xi} \quad && \theta_y = \sum_{i=1}^{n} N_i(\eta,\xi)\theta_{yi} \end{aligned} \tag{10}$$

Here, n represents the number of nodes in the element, which also corresponds to the order of the finite element. The displacement vector is expressed as follows

$$\{d\} = \begin{Bmatrix} u \\ v \\ w \\ \theta_x \\ \theta_y \end{Bmatrix} = \begin{bmatrix} \hat{N} & 0 & 0 & 0 & 0 \\ 0 & \hat{N} & 0 & 0 & 0 \\ 0 & 0 & \hat{N} & 0 & 0 \\ 0 & 0 & 0 & \hat{N} & 0 \\ 0 & 0 & 0 & 0 & \hat{N} \end{bmatrix} \begin{Bmatrix} \hat{u} \\ \hat{v} \\ \hat{w} \\ \hat{\theta}_x \\ \hat{\theta}_y \end{Bmatrix} = [N]\,\{d^e\} \tag{11}$$

The dimension of the interpolation matrix $[N]$ is 5×5n, with, $\hat{u} = \{u_1 \ldots u_n\}^T \hat{v} =$

$$\{v_1 \dots v_n\}^T \hat{w} = \{w_1 \dots w_n\}^T \hat{\theta}_x = \{\theta_{x1} \dots \theta_{xn}\}^T \text{ and } \hat{\theta}_y = \{\theta_{y1} \dots \theta_{yn}\}^T$$

◦ **The stiffness matrix**

Based on the finite element approximation presented in Eq. (10), the strain-displacement matrices (2) are formulated in the same way as in the work of Farhad *et al.* (2018).

$$\begin{aligned} \varepsilon^{(0)} &= D_m u = D_m N d^e = B_m^{(e)} d^e \\ \varepsilon^{(1)} &= D_b u = D_b N d^e = B_b^{(e)} d^e \\ \tilde{a}^{(0)} &= D_s u = D_s N d^e = B_s^{(e)} d^e \end{aligned} \tag{12}$$

Using expressions (10)-(11), the deformation energy Eq. (7) becomes for a single element Ω^e

$$U^e = \frac{1}{2} d^{eT} \int_{\Omega^e} \left\{ B_m^{(e)T} A B_m^{(e)} + B_b^{(e)T} B B_m^{(e)} + B_m^{(e)T} B B_b^{(e)} + B_b^{(e)T} D B_b^{(e)} + B_s^{(e)T} A_s B_s^{(e)} \right\} d\Omega^e d^e \tag{13}$$

Thus, the stiffness matrix of an element (elementary matrix) is obtained by performing the following sum

$$[K]^e = K_{mm}^{(e)} + K_{bm}^{(e)} + K_{mb}^{(e)} + K_{bb}^{(e)} + K_{ss}^{(e)} \tag{14}$$

$$With \qquad K_{mm}^{(e)} = \int_{\Omega^e} B_m^{(e)T} A B_m^{(e)} d\Omega^e \quad K_{bm}^{(e)} = \int_{\Omega^e} B_b^{(e)T} B B_m^{(e)} d\Omega^e$$

$$K_{mb}^{(e)} = \int_{\Omega^e} B_m^{(e)T} B B_b^{(e)} d\Omega^e \quad K_{bb}^{(e)} = \int_{\Omega^e} B_b^{(e)T} D B_b^{(e)} d\Omega^e \quad K_{ss}^{(e)} = \int_{\Omega^e} B_s^{(e)T} A_s B_s^{(e)} d\Omega^e$$

To evaluate the previous integrals we use the natural coordinates (η, ξ), for example the elementary membrane stiffness matrix is $K_{mm}^{(e)} = \int_{-1}^{1} \int_{-1}^{1} B_m^{(e)T} A B_m^{(e)} detJ \, d\xi d\eta$. The Jacobean $J = \begin{bmatrix} \partial x/\partial \xi & \partial y/\partial \xi \\ \partial x/\partial \eta & \partial y/\partial \eta \end{bmatrix}$ is required to pass from the global reference frame (x, y) to the natural reference frame (η, ξ) and $det(J)$ evaluates the determinant of J.

◦ **The mass matrix**

Substituting the finite element approximation (10)-(11) into equation (5), the kinetic energy expression for each element becomes

$$T^e = \frac{1}{2} \dot{d}^{eT} \int_{\Omega^e} N^T [M_I] \, N \, d\Omega^e \, \dot{d}^e \tag{15}$$

Consequently, the elementary mass matrix is obtained according to the following expression

$$[M]^e = \int_{\Omega^e} N^T [M_I] \, N \, d\Omega^e \tag{16}$$

To evaluate the integrals we use the natural coordinates (η, ξ), such as

$$[M]^e = \int_{-1}^{1} \int_{-1}^{1} N^T [M_I] \, N \, detJ \, d\xi d\eta \tag{17}$$

◦ **The geometric rigidity matrix**

The second-order potential energy (9) can be rewritten using the finite element formulation (10) and (11), as follows. For further details, please see Ferreira and Fantuzzi (2020).

$$W_{NL}^{e} = \frac{1}{2} d^{eT} \int_{\Omega^e}^{\cdot} (\nabla N)^T [S_0] \, (\nabla N) \, d\Omega^e \, d^e$$

The gradient matrix ∇ of dimension 10×5.

$$W_{NL}^{e} = \frac{1}{2} d^{eT} \int_{\Omega^e}^{\cdot} G_N^T [S_0] \, G_N d\Omega^e \, d^e \tag{18}$$

Then the geometric rigidity is

$$[G]^e = \int_{\Omega^e}^{\cdot} G_N^T [S_0] G_N d\Omega^e \tag{19}$$

Here, $G_{(N)}$ is a 10×5n matrix corresponding to the derivatives of the shape functions, as shown in Appendix A. To evaluate the integrals of Eq. (19) using natural coordinates: (η, ξ)

$$[G]^e = \int_{-1}^{1} \int_{-1}^{1} G_N^T [S_0] \, G_N det J \, d\xi d\eta \tag{20}$$

4. Structure instability equation

According to the literature, Minh *et al.* (2025), have used an equivalent viscous structural damping of the Rayleigh form, where, we take a linearly dependent damping to the mass and stiffness of the plate. At low frequencies, stiffness dominates. Using the previous concedirations, we write $[C] = \eta \, [K]$. Substituting energies (20), (17) and (14) into principle (4), we obtain the stability equation for an element of the plate under study, as,

According to the literature, Pirmoradian *et al.* (2018) used equivalent viscous structural damping in Rayleigh form, where the damping depends linearly on the mass and stiffness of the plate. Note that, for low frequencies, the stiffness contribution predominates. Taking these considerations into account, we write $[C] = \eta \, [K]$. Substituting the expressions for energies (20), (17) and (14) into principle (4), the stability equation for one element of the plate studied is then written as follows

$$[M]^e \{\ddot{q}\} + [C]^e \{\dot{q}\} + [K]^e \{q\} - P[G]^e \{q\} = 0 \tag{21}$$

After applying an assembly algorithm to the mesh of the entire Ω domain of the plate under study, Eq. (21) becomes

$$[M] \, \{\ddot{q}\} + [C] \, \{\dot{q}\} + [K] \, \{q\} - P[G] \, \{q\} = 0 \tag{22}$$

The matrices [M], [C], [K] and [G] represent the global (N×N dimension) mass, damping, stiffness and geometric matrices respectively, where N corresponds to the total number of degrees of freedom (DOF). Solving Eq. (22) in its complete form for all DOFs can be complex for large matrices ([M], [K], [G]). Consequently, a modal transformation is performed to reduce the size of the problem by retaining only the first most critical mode, i.e., the one excited by the critical buckling load P_{cr} of the plate.

After a few rearrangements, the damping factor for mode number$s$ is

$$\xi_s = \frac{C_n}{2 M_s \omega_s} \tag{23}$$

The problem of the plate's static stability (without taking time t into account) can be reduced to

$$[K] \, \{q\} - P_S [G] \, \{q\} = 0 \tag{24}$$

Eq. (24) is an eigenvalue problem whose solution enables us to determine the critical buckling load P_{cr} that triggers the plate's static instability. In the following, we assume a non-dimensional critical load of the form $\bar{P} = P_{cr}\frac{b^2}{\pi^2 D_{22}}$

For mode number$s$ we determine the natural pulsation ω_s of free vibration without damping under the action of the static load P_s and $\{q\}$ the corresponding mode of natural vibration by solving the following eigenvalue problem

$$([K] - P_s\,[G])\{q\} - \omega_s^2\,[M]\,\{q\} = 0 \tag{25}$$

In practice, we use a non-dimensional form of the natural frequency $\bar{\omega} = \frac{\omega_s b^2}{\pi^2}\sqrt{\frac{\rho h}{D_{22}}}$.

We are developing computer codes under MATLAB to numerically illustrate and evaluate the accuracy and efficiency of the finite element formulation adopted determine the dynamic instability region (DIR) of the plate structure in question. However, to deactivate the shear locking effect, a reduced Gauss quadrature integration scheme (2×2) will be used, while for the menbrane, bending or inertia effects full integration (3×3) will be performed.

5. Solving the problem with Bolotin's approach

Assuming that the dynamic loading of the plate edges is periodic, the study of dynamic instability, according to Shaterzadeh *et al.* (2018) this loading can be modeled as

$$P(t) = P_s + P_d cos\Omega_e t = \alpha P_{cr} + \beta P_{cr} cos\Omega_e t \tag{26}$$

Where, $\alpha = P_s/P_{cr}$, $\beta = P_d/P_{cr}$ are, respectively, static and dynamic load factors that take a quantity between 0 and 1 and Ω_e is the excitation frequency of the dynamic load in the plane. Substituting Eqs. (26) into (22), then

$$[M]\,\{\ddot{q}\} + [C]\,\{\dot{q}\} + [K]\,\{q\} - \alpha P_{cr}[G]\,\{q\} - \beta P_{cr} cos(\Omega_e t)[G]\,\{q\} = 0 \tag{27}$$

Eq. (27) is a collection of "*N*" coupled Mathieu-Hill equations that fully describe the dynamic behavior of the plate. According to Bolotin, this system admits periodic solutions of period T and others of period $2T$ ($T = 2\pi/\Omega_e$). These solutions trace the lower and upper boundaries the secondary and principal dynamic instability regions of the structure in question. Of greater practical importance are the regions of principal instability (DIR) surrounded by periodic solutions of period $2T$.

To get both solutions, Bolotin proposes the following Fourier series forms,
Solutions with period T

$$q(t) = \frac{1}{2}b_0 + \sum_{k=2,4,6,..}^{\infty}\left(a_k sin\frac{k\Omega_e t}{2} + b_k cos\frac{k\Omega_e t}{2}\right) \tag{28}$$

Period solutions $2T$

$$q(t) = \sum_{k=1,3,5,..}^{\infty}\left(a_k sin\frac{k\Omega_e t}{2} + b_k cos\frac{k\Omega_e t}{2}\right) \tag{29}$$

We substitute the two expressions (28) and (29), one after the other, into Eq. (27) and by equalizing the coefficients of sine and cosine this comparison leads us to an infinite system of homogeneous algebraic equations of unknowns a_k and $b_k, k \in \{0,1,2,3,\ldots\}$ $2T$ period solutions

$$\begin{cases}(K+\alpha P_{cr}G-0.5\beta P_{cr}G-0.25\Omega_e^2 M)a_1-0.5\Omega_e C b_1+0.5\beta P_{cr}G a_3=0\\(K+\alpha P_{cr}G+0.5\beta P_{cr}G-0.25\Omega_e^2 M)b_1-0.5\Omega_e C a_1+0.5\beta P_{cr}G b_3=0\\\vdots\end{cases}\tag{30}$$

Solutions with period T

$$\begin{cases}(K+\alpha P_{cr}G)b_0+\beta P_{cr}G b_2=0\\(K+\alpha P_{cr}G-\Omega_e^2 M)a_2-\Omega_e C b_2+\beta P_{cr}G a_4=0\\(K+\alpha P_{cr}G-\Omega_e^2 M)b_2+\Omega_e C a_2+\beta P_{cr}G(2b_0+b_4)=0\\\vdots\end{cases}\tag{31}$$

The two systems of equations above have non-trivial solutions only in the case where the infinite determinants of the corresponding matrices are zero, so we obtain two eigenvalue problems at excitation frequency Ω_e. In practice, we can simplify the infinite problem by taking the first terms into account, so as to have only the most important regions of instability.

$$2T\longmapsto\begin{vmatrix}K+\alpha P_{cr}G-0.5\beta P_{cr}G-0.25\Omega_e^2 M & -0.5\Omega_e \mathrm{C}\\ -0.5\Omega_e \mathrm{C} & K+\alpha P_{cr}G+0.5\beta P_{cr}G-0.25\Omega_e^2 M\end{vmatrix}=0\ for\ k=1{,}3\tag{32}$$

$$T\longmapsto\begin{vmatrix}K+\alpha P_{cr}G-\Omega_e^2 M & 0 & -\Omega_e C\\ 0 & K+\alpha P_{cr}G & \beta P_{cr}G\\ \Omega_e C & 2\beta P_{cr}G & K+\alpha P_{cr}G-\Omega_e^2 M\end{vmatrix}=0\ \ for\ k=0{,}2\tag{30}$$

The study of the dynamic instability of the structure studied, here a moderately thick laminated plate made of composite materials, is generally linked to variations in the parameters, excitation frequency $\Omega_e=\phi\ \omega_s$ and dynamic edge loading factors α and β , with ω_s is the natural frequency of the plate loaded in its plane by P_s. As we can evaluate the instability behavior of the plate aims at the elasticity properties of the materials and also the geometric parameters.

6. Numerical results and interpretation

Considering a symmetrical rectangular laminated structure with angular folds studied in this paper to obtain the limits of dynamic instability regions (DIR), the structure is loaded along two opposite edges by a periodic dynamic load. In all the manipulations that follow, we consider plates of dimension $a\times b\times h$, lamination angle $\theta\in[0°,90°]$ and equal thickness,

$a/b\in[1,2\ 10]$ and $b/h\in[10,20\ 50]$

The properties of the materials used for all layers are:

$E_{11}/E_{22}\in[1,25\ 40]$; $G_{23}=0.5E_{22}$; $G_{13}=G_{12}=0.6E_{22}$; $\nu_{12}=0.25$ and $\rho=1$ kg/m^2

7. Validation of the adopted formulation

Firstly, the proposed iso-parametric finite element formulation was validated by comparing the results obtained with the available literature for one plate, $a/b=1$; $b/h=10$; $E_{11}/E_{22}=1$.

Table 1 Excitation frequency results $\bar{\Omega}_e = \Omega_e a^2 \sqrt{\rho/E_{22}}/h$ for a laminated "SSSS" plate, $(0/90)_{S,2}$ for a static load factor $\alpha = 0.20$ without damping $\xi_n = 0.00$

Refs.	Mesh	Main DIR				Secondary DIR			
		$\beta = 0.1$		$\beta = 0.9$		$\beta = 0.1$		$\beta = 0.9$	
		Ω_e^L	Ω_e^U	Ω_e^L	Ω_e^U	Ω_e^L	Ω_e^U	Ω_e^L	Ω_e^U
Present	10×10	27.9496	29.2826	21.8174	34.0977	14.2809	14.3119	11.5282	14.3119
Present	20×20	31.1194	32.6246	24.1789	38.0547	15.9049	15.9404	12.7432	15.9404
Ref.	///	30.8103	32.3155	23.8698	37.7456	15.5087	15.5442	12.3470	15.5442
Ref.**	///	31.0580	32.5633	24.1176	37.9934	15.2375	15.2731	12.0758	15.2731

*Chakrabarti and Sheikh (2006); **Sahoo and Singh (2015)

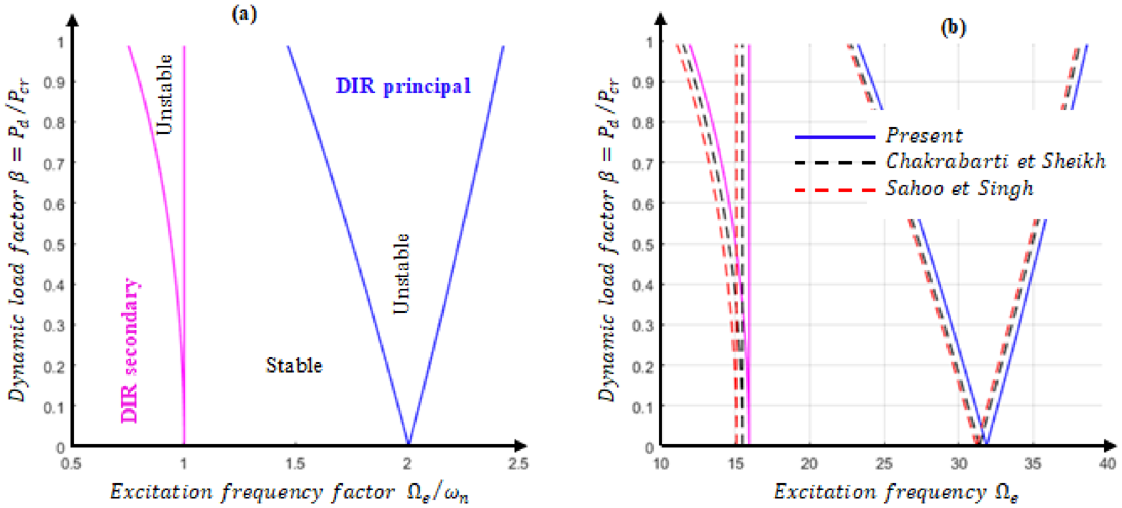

Fig. 4 DIR of the plate studied in Table 1 with a 20×20 mesh (a) secondary and main DIR (b) comparison of the present results with those in the literature

The results obtained in Table 1 are compared with those of Chakrabarti and Sheikh (2006), Sahoo and Singh (2015), as shown in Table 1. This comparison verifies the validity and accuracy of the numerical approach employed. To guarantee the accuracy of the calculations, a 20×20 element mesh was used, showing good convergence of the current results with the reference data. Indeed, the relative deviation remains low, confirming the reliability of the numerical model adopted. In view of this satisfactory convergence, the same mesh has been retained for all the numerical simulations presented in this study, to ensure the consistency and accuracy of the results obtained for different plate configurations.

Fig. 4(a) illustrates the two zones of secondary parametric resonance (DIR) in pink, which represent the dynamic instability of periodic solutions of period T in accordance with Bolotin's approach. In addition, the blue region indicates $2T$-period solutions, highlighting instability domains for different excitation frequencies. This representation provides a better understanding of the periodic instability mechanisms linked to the parametric vibrations of the plate under study.

Fig. 4(b) shows the variation in excitation frequency Ω_e as a function of the dynamic load factor $\beta = P_d/P_{cr}$, where P_d is the applied dynamic load and P_{cr} is the critical buckling load.

Table 2 Natural frequency ω_s of dominant dynamic modes and critical buckling load P_{cr} of N_C -layer constituent plates, with $\theta = 45°$ and $b/h = 10$ and CFCF as boundary conditions

Plate parameters			Natural frequency $\omega_n, n \in \{1,2,3,4,5,6\}$						$P_{cr} \times 10^{-3}$
			Mode 1	Mode 2	Mode 3	Mode 4	Mode 5	Mode 6	
$N_c = 2$	$\frac{E_1}{E_2} = 1$	$a/b = 1$	21.9284	22.1086	27.2379	31.3789	35.6757	36.6483	60.0171
		$a/b = 100$	1.7379	2.8709	3.7530	6.2299	7.0193	9.2568	4.75668
	$\frac{E_1}{E_2} = 25$	$a/b = 1$	32.0171	34.5442	38.0680	42.6611	52.2763	52.5232	15.3277
		$a/b = 100$	2.9576	2.9845	6.0841	7.0658	9.4785	11.5339	1.41592
$N_c = 20$	$\frac{E_1}{E_2} = 1$	$a/b = 1$	21.9337	22.1139	27.2379	31.3815	35.6901	36.6616	60.0314
		$a/b = 100$	1.7381	2.8709	3.7533	6.2303	7.0193	9.2573	4.75706
	$\frac{E_1}{E_2} = 25$	$a/b = 1$	47.6889	47.9478	61.3564	66.6261	69.8242	77.6272	22.8303
		$a/b = 100$	3.1075	5.2846	7.5740	10.5858	12.9368	15.9249	1.48768

This curve compares the results obtained using the formulation proposed in this study (represented by solid lines) with those from two literature references (represented by dotted lines), mentioned earlier.

This comparison highlights the concordance of the results for the primary and secondary instability zones, demonstrating the accuracy and robustness of the numerical approach employed. It also validates the proposed model by comparing it with previous studies, thereby reinforcing the credibility of the analyses carried out in this research.

8. Parametric study of the instability of the plate structure

After the modal transformation carried out previously in order to reduce the size of the problem, we retain the six excited modes with low first frequencies presented in Table 2.

A long-span rectangular bridge deck, characterized by a dimensional ratio $(a/b = 100)$, has lower natural frequencies, which increases the risk of resonance with even low-amplitude excitation forces. This increased susceptibility to vibration is due to the reduced dynamic stiffness associated with the elongated shape of the deck. To mitigate this risk, increasing the number of layers in the structure shifts the first natural frequency, thus delaying the excitation of the plate's first dynamic mode. This multi-layer reinforcement strategy improves dynamic stability while maintaining optimized weight, which is crucial for long-span bridges.

Furthermore, the static stability analysis shows that the structure remains stable as long as the static loading effects on the two opposite sides remain below the critical buckling load $P_{cr} = 60.01\ 10^{-3}\ SI$ in the case of a two-layer laminated square plate. However, this stability threshold decreases considerably for long-span structures with a $(a/b = 100)$ ratio and a high number of layers (over 20), reaching a value of $P_{cr} = 4.75\ 10^{-3}\ SI$. This decrease in the critical threshold is mainly due to the increased flexibility associated with the elongated deck configuration, making the structure more vulnerable to buckling effects and dynamic instabilities. These results underline the importance of careful design of lamination and aspect ratio to ensure both static and dynamic stability of long-span bridge decks.

In the rest of the study, we'll focus on the main DIR, which has the largest opening (see Fig. 4(a)). Fig. 5 is divided into two parts: the first (a) shows the main DIR of a laminated plate with or

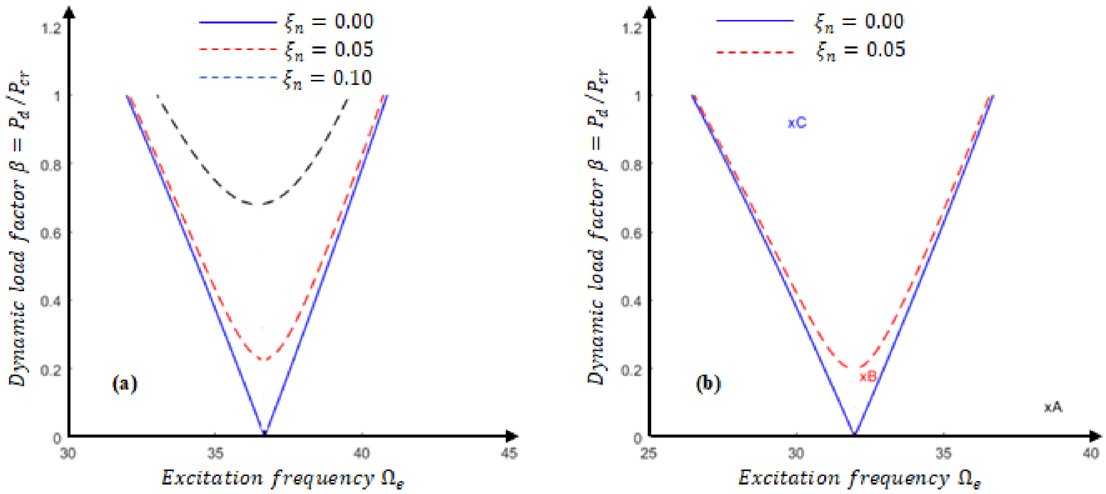

Fig. 6 Main DIR of a laminated plate with $N_C = 2$; $E_1/E_2 = 1$; $\alpha = 0.5$; $b/h = 10$ and $\theta = 45°$, (a) with, or without, damping (b) Three study positions at points A, B and C

without damping $(\xi_n = 0.00, \xi_n = 0.05\ or\ \xi_n = 0.10)$, while the second illustrates the arrangement of three points (A, B and C) where the dynamic behavior of the plate will be determined.

In all configurations studied (whether no damping $\xi_s = 0.00$ or the presence of moderate damping $\xi_n = 0.05$ or greater damping $\xi_s = 0.10$, the opening of the regulated dynamic instability (DIR) region, noted $(\Delta\Omega_e = \Omega_e^U - \Omega_e^L)$, increases with increasing dynamic load factor β. Here, Ω_e^U and Ω_e^L denotes the upper and lower excitation frequencies of the main instability regions, respectively.

In configurations with damping, a minimum value of the dynamic load factor, noted β min, appears. Beyond this threshold, the plate becomes systematically unstable, whatever the applied excitation frequency. This observation indicates the existence of a critical threshold below which damping is sufficient to stabilize the structure, while above this threshold, dynamic effects dominate, leading to instability. Fig. 6(a) also reveals that the value of βmin increases with the damping rate ξ_s. In other words, increasing the damping ratio delays the onset of dynamic instability by raising the critical threshold of the dynamic load factor. This behavior demonstrates the stabilizing influence of damping on plate vibrations, particularly in dynamic regimes where the interaction between excitation frequency and structure response is predominant.

In summary, the study highlights that DIR widening with increasing β is a general feature, but that damping plays a crucial role in defining instability thresholds and modulating the extent of main instability zones.

Using a Runge-Kutta algorithm, Fig. 6 illustrates the time evolution of the response at the structure's center point for three distinct configurations. Configurations A and B are in a zone of dynamic stability, while at point C, the structure exhibits vibratory behavior characterized by a progressively increasing displacement amplitude. This continuous increase in oscillations suggests a phenomenon of dynamic instability, which could eventually lead to deterioration or even failure of the plate if no control measures are applied. Analysis of the trajectories in the associated phase planes reveals distinctive features for each configuration. In particular, point A; shows rapid

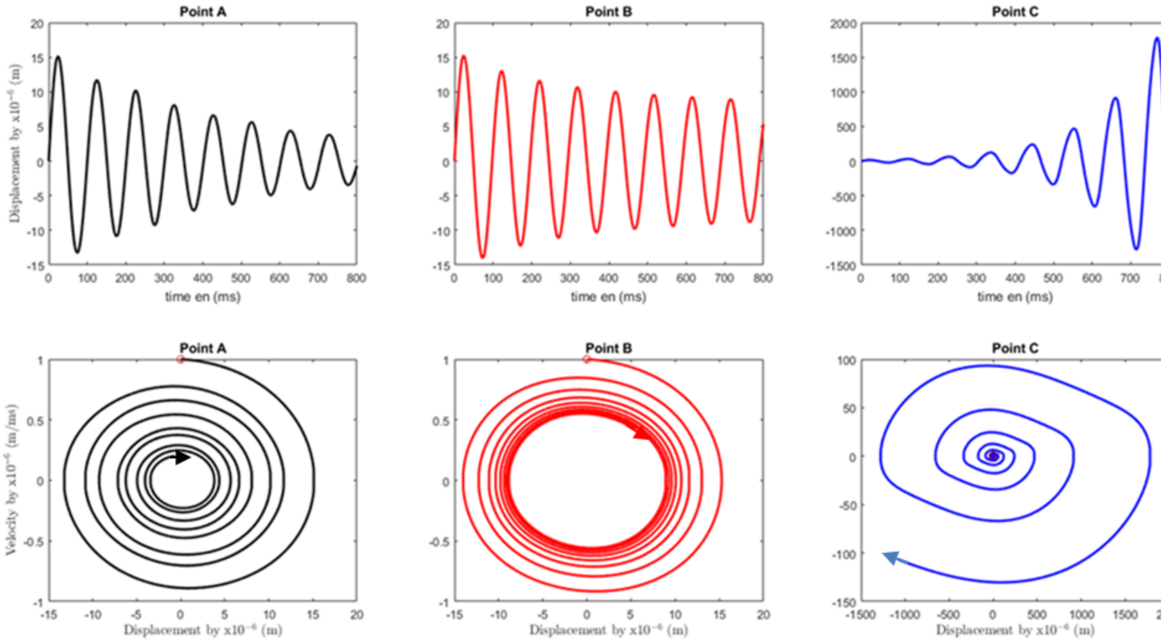

Fig. 6 Displacement versus time and phase plane of the plate studied in Fig. 5 at the three points

convergence towards a stable equilibrium state, indicating effective damping of the initial oscillations. This behavior can be attributed to a favorable combination of dynamic parameters such as dynamic load factor and damping ratio. On the other hand, at point B, although the structure remains in a stable regime, convergence towards equilibrium is slower compared to that observed at A. This suggests a closer proximity to the dynamic instability limit, where excitation effects are less effectively compensated by damping. This observation highlights the sensitivity of the dynamic response to slight variations in loading conditions or material properties. At point C, the absence of displacement stabilization clearly reflects a condition of dynamic instability. Increasing oscillations over time indicate a phenomenon of parametric resonance or non-linear amplification, where excitation energy is continuously transferred to the structure's vibration modes. This behavior can lead to critical stress levels and, ultimately, to structural failure.

In summary, this time-frequency analysis demonstrates the importance of location in the dynamic stability diagram for predicting structural response. Comparison of configurations A, B and C highlights the impact of dynamic load factor and damping on plate vibration stability. These results underline the need for accurate modeling and in-depth analysis to prevent the risk of dynamic instability in sensitive structural applications.

Analyzing the instability of a laminated plate requires assessing the influence of various parameters, such as material properties, notably the anisotropy ratio E_1/E_2, which determines the directional behavior of stiffness. In addition, the geometric characteristics of the plate, such as the aspect ratio a/b and the slenderness ratio a/h, play a crucial role in the dynamic response of the structure. The orientation of the reinforcing fibers, defined by the lamination angle θ, also influences stress distribution and vibration stability. In addition, the diversity of possible boundary conditions, whether simple (S), embedded (C) or free (F), significantly modifies the natural frequencies and vibration modes of the plate. These different parameters have a direct impact on

Table 3 Survey of openings in the instability region $\Delta\Omega_e = \Omega_e^U - \Omega_e^L$ for a laminated plate, with $N_C = 2$ and $\theta = 45°$ and $b/h = 10$ and CFCF as boundary conditions

Damping factor	Aspect ratio	Static load factor $\alpha = 0.2$			Static load factor $\alpha = 0.5$		
		$\frac{E_1}{E_2} = 1$	$\frac{E_1}{E_2} = 25$	$\frac{E_1}{E_2} = 40$	$\frac{E_1}{E_2} = 1$	$\frac{E_1}{E_2} = 25$	$\frac{E_1}{E_2} = 40$
$\xi_n = 0.00$	$a/b = 1$	4.7716	3.4732	3.3646	4.4117	3.1974	3.0933
	$a/b = 2$	7.9383	3.2554	2.9536	7.4759	3.1196	2.8338
	$a/b = 10$	20.6071	53.0160	52.5519	20.0145	47.4407	47.0282
$\xi_n = 0.05$	$a/b = 1$	4.3322	2.8395	2.7057	3.9323	2.4947	2.3597
	$a/b = 2$	7.6822	2.5686	2.1734	7.2034	2.3942	2.0076
	$a/b = 10$	20.5098	52.9783	52.5138	19.9143	47.3985	46.9857

Table 4 Survey of openings in the instability region $\Delta\Omega_e = \Omega_e^U - \Omega_e^L$ for a plate with two types of lamination, with $N_C = 2$; $E_1/E_2 = 1$; $\xi_n = 0.05$; $\alpha = 0.5$ and $b/h = 10$ and CFCF as boundary conditions

Number of layers	θ Regular stratification $(-30°/30°)_{S,N_C}$			θ stratification $(15°/60°)_{S,N_C}$		
	$a/b = 1$	$a/b = 2$	$a/b = 10$	$a/b = 1$	$a/b = 2$	$a/b = 10$
$N_C = 2$	4.1386	6.9376	18.5953	3.7200	5.6282	14.8917
$N_C = 4$	4.1263	6.9274	18.4846	3.7742	5.7721	15.1733
$N_C = 10$	4.1144	6.9193	18.3717	3.8662	6.0574	16.0196
$N_C = 16$	4.1129	6.9183	18.3590	3.8892	6.1258	16.1956
$N_C = 20$	4.1126	6.9180	18.3560	3.8969	6.1501	16.2677

the lower Ω_e^L and upper Ω_e^U boundaries of the main and secondary dynamic instability regions (DIRs). An in-depth study of these effects will help us to better understand the mechanisms of dynamic instability and optimize the design of laminated plates for advanced structural applications.

Table 3 shows the influence of static load factor, anisotropy and aspect ratios and damping factor on the opening $\Delta\Omega_e = \Omega_e^U - \Omega_e^L$ of the main dynamic instability region of the laminated plate $(-45°/45°)_{,1,s}$. The addition of damping stabilizes the structure against low-amplitude dynamic loads, delaying the onset of instability. Dynamic instability appears earlier as the plate becomes more anisotropic (increase in E_1/E_2 for a constant aspect ratio. In addition, the opening of the main DIR is greater for a long-span deck $a/b = 10$. Finally, the effect of damping on this opening is small for dynamic load values β close to 1, but it plays a stabilizing role for lower β.

Table 4 shows symmetrical regulated laminated plate structures $(-30°/30°)_{S,N_C}$ and general $(15°/60°)_{S,N_C}$ of N_C layers parameterized by aspect ratio a/b and number of layers N_C.

Table 4 highlights the impact of the coupling between bending and torsional stiffness D_{16} and D_{26} on dynamic instability. It shows that this coupling has only a negligible influence on the width of the main dynamic instability region (DIR), irrespective of the number of lamination layers in the bridge deck structure. This means that the plate behaves essentially as a superposition of orthotropic layers, allowing the effect of this coupling to be neglected. Furthermore, the table reveals that the general symmetrical lamination $(\theta_1/\theta_2)_{S,N_C}$ offers better stability than the regular symmetrical lamination $(-\theta/\theta)_{S,N_C}$, making it a more advantageous configuration for the bridge deck.

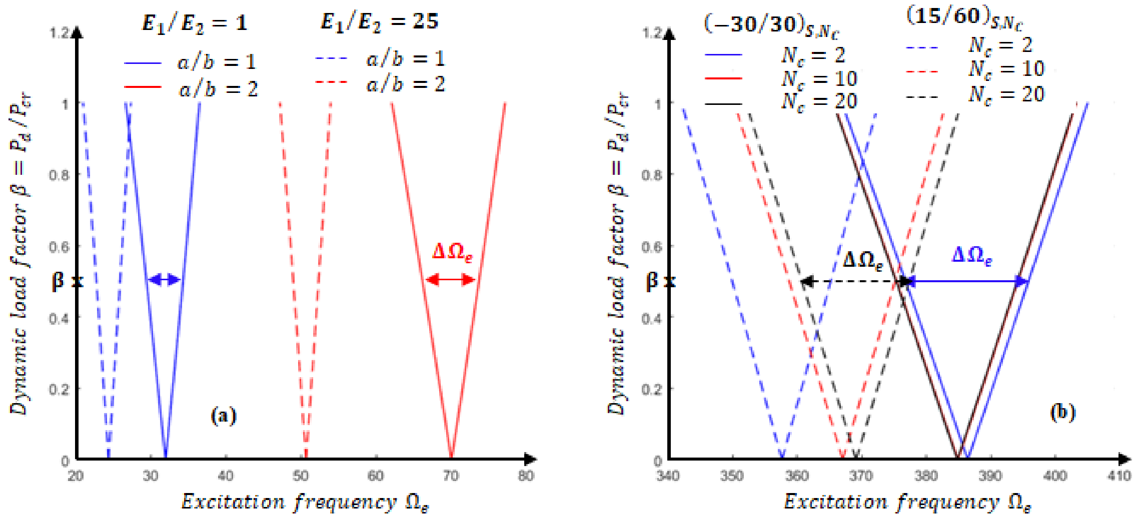

Fig. 8 Main DIR opening for laminated plates, $N_C = 2$; $\alpha = 0$; $\xi_n = 0.00$; $\theta = 30°$; $b/h = 10$ (a) the effect of slenderness and anisotropy ratios (b) the effect of stratification and number of layers

Table 5 Survey of DIR openings $\Delta\Omega_e$ for one plate, with $N_C = 2$; $E_1/E_2 = 1$; $\xi_n = 0.05$; $\alpha = 0.5$; $\theta = 45°$ and $b/h = 10$ and different boundary conditions

Report a/h	XXXX” boundary conditions							
	CFCF		CCCC		SFSF		SSSS	
	$a/b = 1$	$a/b = 2$	$a/b = 1$	$a/b = 2$	$a/b = 1$	$a/b = 2$	$a/b = 1$	$a/b = 2$
$a/h = 10$	4.3322	7.6822	4.0197	1.5902	8.3260	12.2651	8.67834	6.73763
$a/h = 100$	13.0771	39.9022	17.8243	11.6792	38.6320	72.220	37.2727	37.3567

Fig. 8 illustrates the main regions of dynamic instability in the undamped case, considering two different combinations of study parameters.

Dynamic instability appears much earlier for zero static load as the plate becomes more anisotropic (i.e., for higher E_1/E_2 ratios), due to the increased stiffness of the structure, as illustrated in Fig. 8(a). On the other hand, the opening of the main DIR becomes narrower, with $\Delta\Omega_{e_{a/b=10}}(E_1/E_2 = 1) = 20.5098$ being less than $\Delta\Omega_{e_{a/b=10}}(E_1/E_2 = 40) = 52.5138$, as shown in Table 3. Fig. 8(b) also reveals that the dynamic instability of a regular symmetrical laminated plate manifests itself later compared to that of a general symmetrical laminated plate.

Table 5 shows the impact of boundary conditions on the main DIR opening of a symmetrical laminated plate.

The results presented in Table 5 indicate that the opening of the dynamic plate instability increases with the slenderness ratio a/h of the structure. Comparing the effect of embedded connections (C) and single supports (S) on the two opposite edges of the deck, we observe that the boundary conditions (SFSF) make the structure more vulnerable to dynamic instability. On the other hand, the (CCCC) and (SSSS) configurations have no practical relevance for this study, but are mentioned for comparison purposes.

9. Conclusions

This study investigates the dynamic instability of a laminated composite plate subjected to in-plane periodic loading, with or without damping, under various boundary condition configurations. A finite element model based on isoparametric elements was developed, coupled with a time integration scheme using a Runge-Kutta algorithm to simulate the plate's dynamic response.

A key contribution of this work is the realistic modeling of a bridge deck as a symmetric angle-ply laminated composite plate subjected to bilateral dynamic excitation. This loading configuration better captures seismic effects acting on opposite edges, unlike conventional unilateral approaches.

The Reissner-Mindlin (FSDT) theory, incorporating five degrees of freedom per node, was employed to account for transverse shear effects, which are significant in moderately thick structures and typically neglected in classical Kirchhoff-based models.

Using Bolotin's method, the governing equations were reduced to a Mathieu-Hill type system, enabling the identification of primary and secondary instability regions through periodic solutions of period T and 2T. The resulting instability regions revealed that increasing the dynamic load factor widens the instability zone by lowering its lower bound and raising its upper bound. Moreover, regular laminates exhibit delayed onset of instability compared to general laminates. A decrease in anisotropy ratio also delays instability, highlighting the critical role of material properties.

A comprehensive parametric study was carried out, including the effects of Rayleigh damping, number and stacking sequence of layers, anisotropy and slenderness ratios, and various boundary conditions such as CFCF and SFSF. It was found that increasing static load leads to earlier instability onset, and the width of the instability region grows with plate thickness while decreasing with aspect ratio.

Overall, the findings provide valuable insight into the dynamic stability of laminated composite structures and contribute to the optimization of long-span bridge decks under complex dynamic loading. The methodology and results presented serve as a useful reference for the design of dynamically stable composite bridge components subjected to seismic or periodic excitations.

Acknowledgement

The support given to this research project by Sidi Mohamed Ben Abdellah University, Fez, is gratefully acknowledged. The authors would also like to thank the profs. ENS Fès for their help in correcting the manuscript.

Reference

Adhikari, B. and Singh, B.N. (2020), "Parametric instability analysis of laminated composite plate subject to various types of non-uniform periodic in-plane edge load", *Appl. Math. Comput.*, **373**, 125026. https://doi.org/10.1016/j.amc.2019.125026.

Al-Mahdi, A.M. (2020), "Stability result of a viscoelastic plate equation with past history and a logarithmic nonlinearity", *Bound. Value Prob.*, **2020**(1), 84. https://doi.org/10.1186/s13661-020-013829.

Chakrabarti, A. and Sheikh, A.H. (2006), "Dynamic instability of laminated sandwich plates using an efficient finite element model", *Thin Wall. Struct.*, **44**(1), 57-68. https://doi.org/10.1016/j.tws.2005.09.003.

Civalek, Ö., Dastjerdi, S. and Akgöz, B. (2022), "Buckling and free vibrations of CNT-reinforced cross-ply laminated composite plates", *Mech. Bas. Des. Struct. Mach.*, **50**(6), 1914-1931. https://doi.org/10.1080/15397734.2020.1766494.

Dey, P. and Singha, M.K. (2006), "Dynamic stability analysis of composite skew plates subjected to periodic in-plane load", *Thin Wall. Struct*., **44**(9), 937-942. https://doi.org/10.1016/j.tws.2006.08.023.

El Amrani, A., Mataich, H., El-Mekkaoui, J. and El Amrani, B. (2023), "Effect of shear stresses on the deflection and optimal configuration of a rectangular FGM structure", *Couple. Syst. Mech.*, **12**(4), 391-407. https://doi.org/10.12989/csm.2023.12.4.391.

Ferreira, A.J. (2009), *MATLAB Codes for Finite Element Analysis: Solids and Structures*, Springer Netherlands, Dordrecht.

Hoseinzadeh, M. and Rezaeepazhand, J. (2016), "Dynamic stability of laminated composite plates with an external smart damper", *J. Solid Mech.*, **8**(1), 45-57.

Ilyasov, M.H. (2007), "Dynamic stability of viscoelastic plates", *Int. J. Eng. Sci.*, **45**(1), 111-122. https://doi.org/10.1016/j.ijengsci.2006.08.016.

Khodzhaev, D., Abdikarimov, R. and Normuminov, B. (2020), "Dynamic stability of viscoelastic rectangular plates with concentrated masses", *IOP Conf. Ser.: Mater. Sci. Eng.*, **896**(1), 012030. https://doi.org/10.1088/1757-899X/896/1/012030.

Kim, J.H. and Kim, H.S. (2000), "A study on the dynamic stability of plates under a follower force", *Comput. Struct.*, **74**(3), 351-363. https://doi.org/10.1016/S0045-7949(99)00023-1.

Kumar, L.R., Datta, P.K. and Prabhakara, D.L. (2003), "Dynamic instability characteristics of laminated composite plates subjected to partial follower edge load with damping", *Int. J. Mech. Sci.*, **45**(9), 1429-1448. https://doi.org/10.1016/j.ijmecsci.2003.10.008.

Le, C.I., Tran, Q.D., Pham, V.N. and Nguyen, D.K. (2021), "Free vibration and buckling of bidirectional functionally graded sandwich plates using an efficient Q9 element", *Viet. J. Mech.*, **43**(3), 277-295. https://doi.org/10.15625/0866-7136/15981.

Lee, S.Y. (2010), "Finite element dynamic stability analysis of laminated composite skew plates containing cutouts based on HSDT", *Compos. Sci. Technol.*, **70**(8), 1249-1257. https://doi.org/10.1016/j.compscitech.2010.03.013.

Mascolo, I. (2019), "Recent developments in the dynamic stability of elastic structures", *Front. Appl. Math. Statist.*, **5**, 51. http://doi.org/10.3389/fams.2019.00051.

Mataich, H. and El Amrani, B. (2023), "The impact of flexural/torsional coupling on the stability of symmetrical laminated plates", *Eur. J. Comput. Mech.*, 441-466. https://doi.org/10.13052/ejcm2642-2085.3251.

Mataich, H., El Amrani, A. and El Amrani, B. (2024), "Analysis of the thermal instability of laminated composite plates", *Couple. Syst. Mech.*, **13**(2), 95-113. https://doi.org/10.12989/csm.2024.13.2.095.

Mataich, H., El Amrani, A., El Mekkaoui, J. and El Amrani, B. (2024), "Effect of flexure-extension coupling on the elastic instability of a composite laminate plate", *Struct. Eng. Mech.*, **90**(4), 391-401. https://doi.org/10.12989/sem.2024.90.4.391.

Mokhefi, D., Bessaim, A., Houari, M.S.A., Deffane, Z., Houari-Belkadi, H., Ali, B., ... & Merzouki, T. (2024), "A nonlocal strain gradient model for buckling analysis of advanced FG CNT-reinforced composite nanobeams", *Couple. Syst. Mech.*, **13**(5), 375-393. https://doi.org/10.12989/csm.2024.13.5.375.

Ng, L. and Rand, R. (2002), "Bifurcations in a Mathieu equation with cubic nonlinearities: Part II", *Commun. Nonlin. Sci. Numer. Simul.*, **7**(3), 107-121. https://doi.org/10.1016/s1007-5704(02)00018-7.

Nguyen, X.T., Ta, D.H. and Ibrahimbegovic, A. (2024), "Isogeometric analysis of static bending steel UHPC composite slabs based on a refined plate theory", *Couple. Syst. Mech.*, **13**(6), 471-483. https://doi.org/10.12989/csm.2025.13.6.471.

Rajanna, T., Banerjee, S., Desai, Y.M. and Prabhakara, D.L. (2017), "Effect of boundary conditions and non-uniform edge loads on buckling characteristics of laminated composite panels with and without cutout", *Int. J. Comput. Meth. Eng. Sci. Mech.*, **18**(1), 64-76. http://doi.org/10.1080/15502287.2016.1276350.

Reddy, J.N. (2006), *Theory and Analysis of Elastic Plates and Shells*, CRC Press.

Riahi, F., Zirakian, T., Ghaderi, V.M. and Arya, S. (2018), “Buckling stability assessment of plates under uniaxial compression”, *Adv. Sci. Technol.*, **12**(2), 97-105. https://doi.org/10.12913/22998624/90789.

Sahoo, R. and Singh, B.N. (2015), “Dynamic instability of laminated composite and sandwich plates using a new inverse hyperbolic zigzag theory”, *J. Aerosp. Eng.*, **28**(4), 04014109. https://doi.org/10.1061/(ASCE)AS.1943-5525.0000440.

Sahu, S.K. and Datta, P.K. (2007), “Research advances in the dynamic stability behavior of plates and shells: 1987–2005—Part I: Conservative systems”, *Appl. Mech. Rev.*, **60**(2), 65-75. http://doi.org/10.1115/1.2515580.

Shaterzadeh, A., Behzad, H. and Shariyat, M. (2018), “Stability analysis of composite perforated annular sector plates under thermomechanical loading by finite element method”, *Int. J. Struct. Stab. Dyn.*, **18**(07), 1850100.

Singha, M.K. and Daripa, R. (2009), “Nonlinear vibration and dynamic stability analysis of composite plates”, *J. Sound Vib.*, **328**(4-5), 541-554. https://doi.org/10.1016/j.jsv.2009.08.020.

Wang, Y., Wu, H., Yang, F. and Wang, Q. (2021), “An efficient method for vibration and stability analysis of rectangular plates axially moving in fluid”, *Appl. Math. Mech.*, **42**(2), 291-308. https://doi.org/10.1007/s10483-021-2701-5.

Yang, J., Sun, G., Zhou, T. and Yang, J. (2020), “Dynamic stability of piezoelectric plate reinforced with BNNTs considering temperature effect”, *Adv. Compos. Mater.*, **29**(3), 217-233. https://doi.org/10.1080/09243046.2019.1650236.

Yusof, Z., Rasid, Z.A., Hassan, M.Z., Sapuan, S.M., Sarip, S., Yahaya, H. and Yakub, F. (2020), “The parametric instability improvement of fully anisotropic composite plates with embedded shape memory alloy”, *Adv. Compos. Lett.*, **29**, 2633366X19899405. https://doi.org/10.1177/2633366X19899405.

Ziener, C.H., Rückl, M., Kampf, T., Bauer, W.R. and Schlemmer, H.P. (2012), “Mathieu functions for purely imaginary parameters”, *J. Comput. Appl. Math.*, **236**(17), 4513-4524. https://doi.org/10.1016/j.cam.2012.04.023.

Appendix A

Matrices of differential operators

$$[D_m] = \begin{bmatrix} \partial_{,x} & 0 & 0 & 0 & 0 \\ 0 & \partial_{,y} & 0 & 0 & 0 \\ \partial_{,y} & \partial_{,x} & 0 & 0 & 0 \end{bmatrix}, [D_b] = \begin{bmatrix} 0 & 0 & 0 & \partial_{,x} & 0 \\ 0 & 0 & 0 & 0 & \partial_{,y} \\ 0 & 0 & 0 & \partial_{,y} & \partial_{,x} \end{bmatrix} \text{ and } [D_s] = \begin{bmatrix} 0 & 0 & \partial_{,x} & 1 & 0 \\ 0 & 0 & \partial_{,y} & 0 & 1 \end{bmatrix}$$

Material stiffness matrices

$$[\bar{Q}_m]^{(k)} = \begin{bmatrix} \bar{Q}_{11} & \bar{Q}_{12} & \bar{Q}_{16} \\ \bar{Q}_{12} & \bar{Q}_{22} & \bar{Q}_{26} \\ \bar{Q}_{16} & \bar{Q}_{26} & \bar{Q}_{66} \end{bmatrix}^{(k)} \text{ and } [\bar{Q}_s]^{(k)} = \begin{bmatrix} \bar{Q}_{44} & \bar{Q}_{45} \\ \bar{Q}_{45} & \bar{Q}_{55} \end{bmatrix}^{(k)}$$

With,

$$\bar{Q}_{11}^{(k)} = Q_{11}cos^4\theta^{(k)} + 2(Q_{12} + 2Q_{66})cos^2\theta^{(k)}sin^2\theta^{(k)} + Q_{22}sin^4\theta^{(k)}$$

$$\bar{Q}_{12}^{(k)} = Q_{12}cos^4\theta^{(k)} + (Q_{11} + Q_{22} - 4Q_{66})cos^2\theta^{(k)}sin^2\theta^{(k)} + Q_{12}sin^4\theta^{(k)}$$

$$\bar{Q}_{22}^{(k)} = Q_{22}cos^4\theta^{(k)} + 2(Q_{12} + 2Q_{66})cos^2\theta^{(k)}sin^2\theta^{(k)} + Q_{11}sin^4\theta^{(k)}$$

$$\bar{Q}_{16}^{(k)} = (Q_{11} - Q_{12} - 2Q_{66})cos^3\theta^{(k)}sin\theta^{(k)} + \left(2Q_{66}^{(k)} + Q_{12} - Q_{22}\right)cos\theta^{(k)}sin^3\theta^{(k)}$$

$$\bar{Q}_{26}^{(k)} = (Q_{11} - Q_{12} - 2Q_{66})cos\text{è}^{(k)}sin^3\text{è}^{(k)} + (2Q_{66} + Q_{12} - Q_{22})cos^3\text{è}^{(k)}sin\text{è}^{(k)}$$

$$\bar{Q}_{66}^{(k)} = (Q_{11} + Q_{22} - 2Q_{12} - 2Q_{66})cos^2\text{è}^{(k)}sin^2\text{è}^{(k)} + Q_{66}\left(cos^4\text{è}^{(k)} + sin^4\text{è}^{(k)}\right)$$

$$\bar{Q}_{44}^{(k)} = Q_{44}cos^2\text{è}^{(k)} + Q_{55}sin^2\text{è}^{(k)}$$

$$\bar{Q}_{45}^{(k)} = (Q_{55} - Q_{44})\text{cosè}^{(k)}\text{sinè}^{(k)} \quad \bar{Q}_{55}^{(k)} = Q_{55}cos^2\text{è}^{(k)} + Q_{44}sin^2\text{è}^{(k)}$$

The matrix

$$[M_I] = \begin{bmatrix} I_1 & 0 & 0 & I_2 & 0 \\ 0 & I_1 & 0 & 0 & I_2 \\ 0 & 0 & I_1 & 0 & 0 \\ I_2 & 0 & 0 & I_3 & 0 \\ 0 & I_2 & 0 & 0 & I_3 \end{bmatrix}$$

The matrix of non-linear constraints

$$[S_0] = \begin{bmatrix} h\hat{\text{ô}}_0 & 0 & 0 & 0 & 0 \\ 0 & h\hat{\text{ô}}_0 & 0 & 0 & 0 \\ 0 & 0 & h\hat{\text{ô}}_0 & 0 & 0 \\ 0 & 0 & 0 & \hat{\text{ô}}_0\, h^3/12 & 0 \\ 0 & 0 & 0 & 0 & \hat{\text{ô}}_0\, h^3/12 \end{bmatrix}$$

The matrix of shape function derivatives for the geometric matrix

$$G_N = \begin{bmatrix} N_{,x} & 0 & 0 & 0 & 0 \\ N_{,y} & 0 & 0 & 0 & 0 \\ 0 & N_{,x} & 0 & 0 & 0 \\ 0 & N_{,y} & 0 & 0 & 0 \\ 0 & 0 & N_{,x} & 0 & 0 \\ 0 & 0 & N_{,y} & 0 & 0 \\ 0 & 0 & 0 & N_{,x} & 0 \\ 0 & 0 & 0 & N_{,y} & 0 \\ 0 & 0 & 0 & 0 & N_{,x} \\ 0 & 0 & 0 & 0 & N_{,y} \end{bmatrix}.$$